AFRL-RV-PS-
TR-2019-0138

PINPOINTING SEISMIC EVENTS WITH BODY WAVES SCATTERED BY TOPOGRAPHY NEAR THE SOURCE REGION

Yang Shen, et al.

University of Rhode Island
215 South Ferry Road
Narragansett, RI 02818

30 June 2019

Final Report

AIR FORCE RESEARCH LABORATORY
Space Vehicles Directorate
3550 Aberdeen Ave SE
AIR FORCE MATERIEL COMMAND
KIRTLAND AIR FORCE BASE, NM 87117-5776

DTIC COPY

NOTICE AND SIGNATURE PAGE

AFRL-RV-PS-TR-2019-0138 HAS BEEN REVIEWED AND IS APPROVED FOR PUBLICATION IN ACCORDANCE WITH ASSIGNED DISTRIBUTION STATEMENT.

//SIGNED//	//SIGNED//
Dr. Frederick Schult Program Manager, AFRL/RVB	Dr. Thomas R. Caudill, Chief AFRL Geospace Technologies Division

REPORT DOCUMENTATION PAGE

Form Approved
OMB No. 0704-0188

1. REPORT DATE *(DD-MM-YYYY)*	**2. REPORT TYPE**	**3. DATES COVERED** *(From - To)*
30-06-2019	Final Report	31 May 2017 – 30 Jun 2019

4. TITLE AND SUBTITLE
Pinpointing Seismic Events with Body Waves Scattered by Topography Near the Source Region

5a. CONTRACT NUMBER
FA9453-17-C-0026

5b. GRANT NUMBER

5c. PROGRAM ELEMENT NUMBER
62601F

6. AUTHOR(S)
Yang Shen, Nian Wang, and Xueyang Bao

5d. PROJECT NUMBER
1010

5e. TASK NUMBER
EF129471

5f. WORK UNIT NUMBER
V134

7. PERFORMING ORGANIZATION NAME(S) AND ADDRESS(ES)
University of Rhode Island
215 South Ferry Road
Narragansett, RI 02818

8. PERFORMING ORGANIZATION REPORT NUMBER

9. SPONSORING / MONITORING AGENCY NAME(S) AND ADDRESS(ES)
Air Force Research Laboratory
Space Vehicles Directorate
3550 Aberdeen Avenue SE
Kirtland AFB, NM 87117-5776

10. SPONSOR/MONITOR'S ACRONYM(S)
AFRL/RVBN

11. SPONSOR/MONITOR'S REPORT NUMBER(S)
AFRL-RV-PS-TR-2019-0138

12. DISTRIBUTION / AVAILABILITY STATEMENT
Approved for public release; distribution is unlimited (AFMC-2019-0647 dtd 25 Oct 2019).

13. SUPPLEMENTARY NOTES

14. ABSTRACT
This contract explores the power and limitation of a novel, seismic event location method based on waves scattered by surface topography. We validated this method, using seismic data from the 1993 Non-Proliferation Experiment, a chemical explosion with a precisely known location at the Nevada Test Sites, a region with moderate topography. We explored the effects of velocity heterogeneity, signal frequencies, time windows and other factors on the scattered waves and estimated locations. We applied this method to the Sept. 3rd 2017 DPRK nuclear test, using records from four seismic stations in China and South Korea. The solution is within 1 km of those of several other studies. We also studied the effects of 3D velocity models on full-wave moment tensor solutions of the DPRK nuclear tests. The moment tensor solutions show a dominant isotropic component, as expected from explosions, though there are also notable non-isotropic components. The event following the explosion contained mainly an implosive component, consistent with a tunnel collapse.

15. SUBJECT TERMS
topography scattered waves, seismic event location, absolute versus relative locations, full-wave moment solutions

16. SECURITY CLASSIFICATION OF:			**17. LIMITATION OF ABSTRACT**	**18. NUMBER OF PAGES**	**19a. NAME OF RESPONSIBLE PERSON**
a. REPORT	**b. ABSTRACT**	**c. THIS PAGE**			Dr. Frederick Schult
Unclassified	Unclassified	Unclassified	Unlimited	42	**19b. TELEPHONE NUMBER** *(include area code)*

This page is intentionally left blank.

Table of Contents

List of Figures

This page is intentionally left blank.

1. SUMMARY

The main objective of this contract is to explore the power and limitation of a novel, seismic event location method based on waves scattered by surface topography. Using numerical experiments, we showed previously that waves scattered by surface topography can be used to accurately locate shallow seismic events in places with significant topographic relief. To validate this method, we used seismic data from the 1993 Non-Proliferation Experiment (NPE), a chemical explosion with a precisely known location at the Nevada Test Sites, an area with low to moderate topographic relief. We located the NPE explosion by comparing the observed broadband waveforms at regional distances with synthetic waveforms (Wang et al., 2019). We explored the effects of velocity heterogeneity, signal frequency, time window length and other factors on the scattered waves and location solutions. This topography-scattered-wave-based method successfully locates the source within 0.5 km of the true location. We conclude that this method is effective for determining the absolute (as opposed to relative) hypocenter location when applied to real seismic datasets, even for a small number of seismic stations distributed in a poor source-receiver geometry as in this validation case.

Application of this method to the September 3, 2017 DPRK nuclear test using four stations in China and South Korea yielded a location solution within 1 km of the locations of several other studies. Using the Green's functions based on a 3D velocity model (Pasyanos et al., 2014), we inverted the moment tensor of the September 3, 2017 DPRK nuclear test. The results show that there is a significant compensated linear vector dipole (CLVD) component (31%) and a double couple (DC) component (14%) in the moment tensor.

2. INTRODUCTION

Accurate locations of seismic events are essential to discrimination of earthquakes and explosions. They are also fundamental in a wide range of seismological studies, including moment tensor inversion, yield estimation and source characterization, and development of velocity and attenuation models. In the past several decades, location studies have used ray theory and travel times of seismic arrivals. The prediction of travel times depends on velocity models, which are almost always inaccurate and uncertain. This uncertainty leads to errors in source locations. In particular, the source depth, a key piece of information in source characterization and discrimination, is often poorly resolved because of the lack of stations near the source in the domain of underground nuclear test monitoring. The relative location methods (e.g., Waldhauser and Ellsworth, 2000; Schaff and Richards, 2004; Selby, 2010; Wen and Long, 2010; Murphy et al., 2013; Zhao et al., 2014, 2016; Pasyanos and Myers, 2018) can greatly improve relative locations of seismic events, but not absolute locations.

In contrast, the Earth's surface, the largest velocity interface for seismic waves, is often precisely known at the scale of seismic wavelengths (> 100s m). Wave scattering near the source converts the near-field evanescent waves to propagating waves in the far-field, which can be used to achieve location accuracy beyond the diffraction limit (Lerosey et al., 2007). For shallow sources in regions with significant topography, such as underground explosions or shallow volcanic earthquakes, scattering by topography could be the dominant mechanism that

produces scattered waves (e.g., Kennett, 1987; Stead and Helmberger, 1988; Gupta et al., 1991; O'Brien and Bean, 2009; Rodgers et al., 2010; Imperatori and Mai, 2015). Amplitude of topography scattered waves can be comparable to that of the direct arrival in some azimuths (Stevens and O'Brien, 2018).

Using models with realistic surface topography and synthetic seismic sources, we demonstrated that waves scattered by surface topography can be used to achieve accurate source locations with robust determination of the source depth (Wang et al., 2016). The method is insensitive to uncertainties in the velocity model as the synthetic waveforms generated at trial locations are cross-correlated with the "data" and time-shifted to mitigate the effect of an inaccurate velocity model. Because the P-coda waves of shallow events are dominated by topographic scattering, variations in the scattered waveforms provide information to determine the absolute (as opposed to relative) location of the source. The solution remains robust with a wide range of random noises in data, un-modeled random velocity heterogeneities, and uncertainties in moment tensors. The method can be extended to locate pairs of sources in close proximity by using differential waveforms to further reduce errors due to un-modeled velocity structures.

In this contract, we explored further the power and limitation of this waveform-based location method, validated it with observations from a known explosive source, and applied it to the North Korea nuclear tests.

3. TECHNICAL APPROACH AND RESULTS

3.1 Validation of the Location Method Based on Topography Scattered Waves

To validate the method of Wang et al. (2016), we use observed waveforms from the Non-Proliferation Experiment at the Nevada Test Sites on September 22, 1993 (Denny and Zucca, 1994; Tinker and Wallace, 1997). The location of this chemical explosion is precisely known (longitude −116.20986°, latitude 37.20193°, and 390 m below the surface) and is referred to as S_0 hereinafter (Figure 1). We use the three-component seismograms at 12 broadband stations located about 50-150 km away from the source as the data. Through amplitude spectrum analysis and signal noise ratio analysis of the data (in the time window 5 s before its first arrival and 3 s after its first arrival), we find that the appropriate frequency band to investigate the first arrivals and their coda waves is between [1.0 3.0] Hz (Figure 2).

In the following sections, we describe the forward simulation of wave propagation, compare the synthetics with the data, and introduce the source location method. Then we show the solution for the Non-Proliferation Experiment in the Nevada Test Sites using P and P coda waves. Finally, by adding stochastic velocity heterogeneities in the velocity model without topography, we assess the relative contributions of topography versus velocity heterogeneities on scattered waves used for locating shallow sources. Wang et al. (2019) provides additional details of this validation study.

3.1.1 Forward Wave Propagation Simulations

We use a 3D collocated-grid finite-difference method (Zhang and Chen, 2006; Zhang *et al.*, 2012) to generate synthetic seismograms at the 12 stations (Figure 1). The reference model including density and velocity structures is taken from CRUST 1.0 (Laske *et al.*, 2013). Surface topography constructed from high resolution (~10 m) elevation data from the USGS National Map Viewer platform (http://viewer.nationalmap.gov/viewer/) is added to the model for precise simulation of waves scattered by surface topography. For computational reasons, we divide the computation into two regions (noted as C1 and C2) that contain the chemical explosion source and the 12 stations (Figure 1a). The depth range for the simulations is from the surface down to z = −100 km in the mantle, where z = 0 is the sea level. We use a grid size of $\Delta x=\Delta y=125$ m in the x and y (horizontal) directions, and a variable grid size in the z (vertical) direction, which changes from about 160 m near the surface to 2 km near the bottom of the model. We down-sample the original elevation data to 125 m in the x-y plane. The down-sampled elevation still maintains the character of the original topography as the lateral scales of the main topography is much large than the grid size. The collocated-grid finite-difference method needs eight points-per-wavelength for accurate simulation of body-wave propagation (Zhang et al., 2012), so the minimum wavelength is 8×125 m = 1 km. This ensures correct body wave seismograms at frequencies up to 3 Hz (3 km/s / 1 km = 3 Hz, assuming the minimum wave speed of 3 km/s). The temporal increment in wave simulation is $\Delta t=5\times10^{-3}$ s. The source is an explosive source that acts on the stress terms. The time function of its moment (not the moment rate) is a bell integral function with a full duration of 0.1 s. It takes about 4 hours wall-clock time for each simulation (with 10^4 time steps) using 160 CPU cores on a Linux cluster at the University of Rhode Island.

To test the sensitivity of synthetic seismograms on the location of the source, we compare seismograms generated by different test sources near S_0. The relative locations of the test sources and the slices of the P-wave velocity around S_0 are shown in Figure 3. We find obvious differences in seismograms generated at different test locations when surface topography exists (Figure 4). In contrast, the seismograms do not vary much in the model with a flat free surface. This demonstrates that the waveforms are sensitive to the source location in the model with surface topography. Figure 5 shows a comparison between the data and the synthetic waveforms calculated in the models with and without topography.

Although the classification of the first arrival is nonconsequential for the event location, to facilitate discussion we identify the first arrivals as Pg waves at stations AZ07-AZ10, and Pn waves at the other stations, based on the prediction of the software Taup (Crotwell, et al., 1999) using the reference model ak135 (Kennett *et al.*, 1995). By comparing the synthetics using the models with and without topography, we find that topography not only generates scattered waves in the coda but also modifies the waveforms of the first arrivals (Pn/Pg waves). The waveform match between the observed and the synthetic for the test location S_0 varies from station to station (Figure 5). At stations AZ01 and AZ03, the synthetics match the data well both in phase and amplitude. At other stations, the synthetics match the data well in phase, but there are differences in amplitude (Figure 5), which may be due to the imperfection of the velocity model and the complexity of the source.

At each station, we choose the time-window of the waveform so that it contains the first arrival and its immediate coda, excluding the second main arrival as predicted by Taup (Crotwell, et al., 1999). We do not use the second arrival as the interference of the second arrival with the coda of the first arrival leads to additional complexity. The exact length of the selected

time window is based on an initial comparison between the data and synthetics, where we calculate the cross-correlation coefficients in increasingly larger time windows, which start from 0.5-1 s before the first arrival and end before the predicted arrival time of the second arrival or 2.0 s after the first arrival, whichever comes first. As the length of the time window increases, the difference of waveforms between the data and synthetic seismogram generally becomes larger and the cross-correlation coefficients decrease for the test sources. We set a threshold of the cross-correlation coefficient (equal to 0.8) to choose the time window for the hypocenter inversion. The cross-correlation coefficients vary slightly for different initial test sources but the length of the chosen time window at each station is insensitive to the choice of the test sources when the time window is limited to before the second arrival. Under these conditions, the chosen coda waves are about 0.5 - 1.0 s after the P waves, and these short time windows effectively limit the region contributing to topographic scattering to the area directly above the source.

3.1.2 The Full Waveform Source Location Method

We use the full waveform source location method proposed by Wang *et al.*, (2016), which is a non-linear grid-search method (Sambridge and Kennett, 1986; Lomax *et al.*, 2008) combined with the strain Green's tensor database (Zhao *et al.*, 2006), to locate the Non-Proliferation Experiment in the Nevada Test Sites. The strain Green's tensor is obtained by applying a point and impulsive force acting in the x, y, and z directions separately at each station. For each grid in the search volume (its coordinate is [103.875 km, 113.875 km] × [105.5 km, 115.5 km] in the horizontal (x-y) plane, and [-8.07 km, surface km] in the vertical (z) direction, which contains 41×41×24 grids, Figure 1), we calculate the synthetics at the stations by convolving its strain Green's tensor with the equivalent explosive source moment tensor (Kikuchi and Kanamori, 1991) using source-receiver reciprocity. In this way, we only need to do 3N times simulations (N is the number of stations, so N=12 in this study) instead of forty thousand forward simulations for all the grids in the search volume (41×41×24=40344 grids), which is extremely computational efficient. We note that our best solution does not depend on the starting test source location since we use a global, non-linear grid search (Wang *et al.*, 2016).

We use seismograms in the frequency band of 1.0-2.0 Hz, which have good signal-to-noise ratios, relatively low source-time complexity, and moderate topography scattered waves (Figure. 2). The results in the frequency band of 1.0-3.0 Hz are provided in discussion later. At a higher frequency, scattering is stronger, but it needs a finer grid and a smaller time step for the simulation, increasing the computational costs. As a rule of thumb, increasing the wave frequency by a factor of 2 increases the computational cost by ~16 times.

We normalize and align the data and synthetics, using cross correlation to highlight the waveform difference due to scattering. The amplitude normalization and time shift are necessary as the velocity and attenuation models are not perfectly known. Because of the normalization and time shift in waveforms, we only invert the hypocenter of the explosion and ignore other parameters such as the magnitude and origin time. Then, we calculate the least-squares waveform misfit of the normalized and time-shifted waveforms (eq. (1)) to find the solution that yields the minimum waveform misfit. Furthermore, to deal with random noise in real data, we use a weighting technique to calculate the optimal weighting coefficients (Brown *et al.*, 1977).

The L_2-norm waveform misfit between the data and synthetic seismograms is defined as

$$E(sp) = \sum_{j=1}^{3}\sum_{i=1}^{N} w_i^j \frac{1}{t_2 - t_1}\int_{t_1}^{t_2} (y_i^j(t - \delta t_i^j) - obs_i^j(t))^2 dt, \quad i = 1,\ 2, \ldots, N,\ \ j = 1,\ 2,\ 3 \qquad (1)$$

where $y_i^j(t)$ is the synthetic seismogram at the *i*th station ($1 \le i \le N$) and for the *j*th ($1 \le j \le 3$) component generated by a source located at sp=(x, y, z), and $obs_i^j(t)$ is the observation at the *i*th station and for the *j*th component. N is the total number of stations. (t_1, t_2) is the time window of the seismogram chosen to calculate the misfit. δt_i^j is the time shift to align the waveforms after cross correlation between the observed and synthetic seismograms. w_i^j is the weighting factor, which is based on the quality of the data and the cross-correlation coefficient between the synthetic seismogram and data. To compute the optimal weighting coefficients (Brown *et al.*, 1977), we calculate the signal-to-noise ratio as $\gamma_i^j = \sigma_{si}^j / (\sigma_{ni}^j)^2$, where σ_{ni}^j is the standard deviation of the noise and σ_{si}^j is the standard deviation of the signal. The time window of the noise is 5 s before the first arrival time, and the time window of the signal is between the first arrival and 3.5 s after the first arrival time. Then, we obtain the weighting factor as $w_i^j = \gamma_i^j / \sum_{j=1}^{3} \gamma_i^j$ at each station and for each component.

From the least-squares misfit between the data and synthetics, we obtain the best solution that is the global minimum in the grid search volume. For the posteriori error estimation of the best solution sp*, we can calculate its confidence interval sp$\in$[spa, spb] at the given level of confidence C (e.g., C=95%), such that the relative misfit error $ER(sp) = (E(sp) - E(sp^*)) / E(sp^*)$ satisfies

$$ER(sp) = (E(sp) - E(sp^*)) / E(sp^*) \le p \times F_{R-p}^p(C) / (R - p), \quad p=3,\ R=3N \qquad (2)$$

where F_{R-p}^p is the Fisher distribution (Draper and Smith, 1966) with p and (R-p) degrees of freedom. We take p=3 since we only locate hypocenter of the source, and we take R=3N since we use three components of seismograms at each station. By calculating the minimum and maximum values (the upper and lower bounds) of all possible solutions (of sp) satisfying the condition in equation (2), we get the confidence interval indicating the uncertainty of the best solution.

3.1.3 Results and Discussion

Figure 6 shows the misfit E for the test sources in the search volume on the three surfaces cut at the best solution along the x-z plane, the y-z plane, and the x-y plane, using P only waves (Figure 6a) and P plus the coda waves (Figure 6b). In both cases, the misfit is elongated in the y direction, reflecting a lack of stations in the north and south directions of the source. In the vertical direction, the misfit for P and the coda has several local minima (Figure 6b), indicating scattering causes strong non-linearity in the misfit and the necessity of a global search method as used in this study. The misfit of P only also has local minima, but it is smoother and has a broader minimum misfit space (Figure 6a), suggesting that the misfit of P wave has a relatively weaker nonlinearity but a higher uncertainty of the solution. Indeed, when scattered coda waves

are incorporated, the distance between the known source and the inverted source is improved from 1.0 km to 0.25 km in the x direction, from 1.25 km to 0.25 km in the y direction, and from 0.6 km to 0.14 km in the z direction. The uncertainty of the solution at the one standard deviation level (C=68%, in eq. (2)) is reduced from 0.875 km to 0.25 km in the x direction, from 1.0 km to 0.875 km in the y direction, and from 0.31 km to 0.16 km in the z direction (Table 1). For comparison, the location results using P and P coda waves in the frequency band of [1.0 3.0] Hz are shown in Figure 7. We observe that S_0 is between the two best location solutions in the two frequency bands, indicating the effect of the choice of the frequency band on source location. However, the two best solutions are within 0.5 km of S_0 in the horizontal (x-y) plane, illustrating the robustness of this location method. The uncertainty of the best location in the frequency band of [1.0 3.0] Hz is 0.625 km in the x and y directions and 0.32 km in the z direction.

The source region has significant variations in elevation (Figure 1b), which causes substantial scattering as shown in Figure 4. In the frequency band we use (1.0-3.0 Hz), the signal to noise ratio is high (Figure 2). Comparing the level of noise to the waveform difference due to topography (Figure 5), it is clear that the effect of wave scattering by topography is much stronger than random noise in the data in this case. Thus, random noise in this study likely has a negligible effect on the location solution in the frequency band we use.

The velocity model (CRUST 1.0) used to generate synthetic waveforms is a relatively coarse model that does not represent small-scale heterogeneities in the Earth (Goff et al., 1994), which also cause wave scattering. So, it is necessary to assess the relative contributions of topography versus velocity heterogeneities to scattered waves used in source location. In the computational region C2, based on the reference model without surface topography, we add stochastic velocity heterogeneities characterized by the von Kármán-type power spectral density (PSD) function (Goff *et al.*, 1994, Wang *et al.*, 2016). We set the scales of the heterogeneities at 10 km, which are comparable to the wavelengths of P waves at ~1-2 Hz. The percentage of P- and S-wave velocity perturbations gradually increases from 1% up to 10%. We calculate synthetics in the perturbed and unperturbed models without surface topography and obtain their waveform differences as the volumetric velocity perturbations changes. As expected, scattering is enhanced by the velocity heterogeneities especially for the x and y components of the seismograms. However, scattering by velocity heterogeneities is quite different from scattering by topography (e.g., Imperatori and Mai, 2015; Takemura et al., 2015) as seen on Pg and Pn coda waves (Figure 8). We investigate the overall waveform misfit (eq. (1)) at different levels of velocity heterogeneities and compare it with the effect of surface topography (the waveform differences between the unperturbed models with and without topography) (Figure 9). Specifically, we compute the misfit of Pg and Pg coda waves at four stations (AZ07-AZ10) (Figure 9b), Pn and Pn coda waves at other eight stations (Figure 9a), and the misfit of the first arrivals and their coda waves at all the twelve stations (Figure 9c). Overall, topography scattering is dominant, but as the velocity perturbation percentage increases towards 10%, velocity perturbations may produce comparable misfit to that produced by topography (Figure 9). We note that this relative importance in scattered waves varies with roughness of surface topography, source depth, and wave frequency. In places with rougher topography and shallower sources, for example, topographic scattering is expected to be stronger. Conversely in places with little surface topography and deep sources, topographic effects would be small. Thus, this kind of analysis is needed in each particular case (Wang et al., 2019).

Finally, we note that as a grid search method, our approach requires that the search volume encompasses the true source location. Given the high computational cost of the full waveform methods, it is often appropriate to obtain an initial location using travel-time based methods. Because of the highly nonlinear nature of wave scattering by topography (Figure. 6), the better the initial solution from other methods, the more likely the full-wave-based search will be able to find the global minimum misfit solution. We conclude that the location method using waves scattered by topography is effective for the hypocenter location when applied to real seismic datasets, even though only 12 stations are available and the source-receiver coverage is not ideal (a lack of stations in the y-direction). Further validation of the method for a wide range of topographic roughness and source depth is desirable.

3.2 Location of the Sept. 3rd 2017 DPRK Test

On September 3, 2017, North Korea conducted its sixth and by far the largest nuclear test at the Punggye-ri test site. We applied our location method based on waves scattered by topography to locate this event. In the computational region around the North Korea nuclear test site (Figure 10b), we perform forward waveform modeling, and we use the first arrivals (Pn waves) and their immediate codas at stations to pinpoint the source location, following the method of Wang et al. (2016, 2019).

Figure 11 shows the comparison of seismograms at the four stations generated in the models with and without topography, where the test source is located at the Punggye-ri test site (the yellow point in Figure 10). P coda waves are excited in the topographic model, which are likely dominated by waves scattered by the surface topography near the source. This is supported by nonlinear finite-element modeling of seismic waves generated by the explosion (Stevens and O'Brien, 2018). The synthetic waveforms and the data fit relatively well on Pn waves and vary on the immediate Pn coda waves (Figure 12), indicating the inaccuracy of the test location as well as the reference velocity model.

We assess the solution in the search volume using the least-squares misfit between the observed and synthetic waveforms. Figure 13 illustrates the contour plots of the misfit between the observed and synthetics for the September 3, 2017 event in the x-z and y-z planes cut at the location of the best solution (latitude 41.308°, and longitude 129.067°). The dark blue region indicates the one standard deviation range of the misfit of the best solution. The one standard deviation uncertainty as the posterior error estimation is (0.4 km, 0.5 km, 0.0667 km) in the latitude, longitude, and vertical directions. For comparison, we also show the 3D view of epicenter locations obtained by our study and other studies based on relative travel times such as the USTC solution (latitude 41.2982°, and longitude 129.0742°) and NORSAR solution (latitude 41.2994°, and longitude 129.0789°) (Figure 14). The three locations are within 1 km between each other in the latitude and longitude directions. Our results show that the waveform-based location method allows us to obtain accurate solutions with a small number of stations. The solutions are absolute locations (with associated errors) as opposed to relative locations based on relative travel times, because topography-scattered waves depend on the geometric relations between the source and the unique topography near the source.

Figure 15 shows the results of using both differential waveforms and travel-times to locate the North Korea tests in years 2016 and 2017 as a pair to further reduce the effects of inaccuracies in the reference velocity model (CRUST 1.0).

3.3 Full-Wave Moment Tensor Solutions of the Sept. 3rd 2017 DPRK Test

Accurate estimation of the source moment and its uncertainty is important for discriminating underground explosions from earthquakes (e.g., Ford et al., 2009) and estimating the yields of nuclear explosions. In this study, we determine the full moment tensor of the September 3, 2017 nuclear test by the Democratic People's Republic of Korea (DPRK) at the Punggye-ri test site.

We use waveform data recorded at broadband seismic stations located in China, South Korea, and Japan (Figure 16). Applying a non-staggered-grid, finite-difference algorithm, we calculate strain Green's tensors (SGTs) based on a 3D Earth model LITHO1.0 (Pasyanos et al., 2014) overlying a 1D reference model AK135 (Kennett et al., 1995). Taking advantage of the source-receiver reciprocity, this SGT database was pre-calculated and stored for the Punggye-ri test site. In the inversion for source moment tensors, we employ the source location estimated from regional Pn and Pn-coda waveforms in our recent study (Wang et al., 2017a).

In order to determine the moment tensor solution and its uncertainty, we adapt the method of Alvizuri and Tape (2016) in a grid search over a 6-D model space of the moment tensor: the scalar moment magnitude, the source type in the lune diagram (Tape and Tape, 2012), and the moment tensor orientation represented by the strike, dip, and rake angles (Table 2). M_{w0} is an initial moment magnitude estimated using the method of Zhou et al. (2016).

For each moment tensor $\boldsymbol{M}$ defined by the six parameters, the synthetic displacement seismogram is calculated by

$$u_n^m = \boldsymbol{G}_n(r_s, t; r_r): \boldsymbol{M} * S(t, r_s), \tag{3}$$

where $\boldsymbol{G}_{\mathrm{n}}$ is the *n*th component Green's function from station r_r to the source r_s, S is the source time function. We follow the "cut-and-paste" algorithm (e.g., Zhu and Helmberger, 1996) and calculate the waveform misfit between the observed and synthetic seismograms. The misfit function is defined as

$$\Phi = \sum_{k=1}^{N_t}\sum_{j=1}^{N_f}\sum_{i=1}^{N_w}\left[w_{ijk}\frac{\left(u_{ijk}^{obs}-u_{ijk}^{syn}\right)^2}{\left(u_{ijk}^{obs}\right)^2}\right]\Big/\sum_{k=1}^{N_t}\sum_{j=1}^{N_f}\sum_{i=1}^{N_w} w_{ijk}, \tag{4}$$

where N_{t}, N_{f}, N_{w} denote the number of traces, the number of frequency bands, and the number of phases, respectively. Superscripts *obs* and *syn* denote the observation and synthetics, respectively. W_{ijk} is the weighting factor determined based on the noise level. The variation of misfit Φ is plotted in the lune diagram. The optimal moment tensor at a lune coordinate (δ_0, γ_0) is defined as

$$\Phi_m(\delta_0, \gamma_0) = min[\Phi(M_w, \delta_0, \gamma_0, \kappa, \sigma, \theta)] \tag{5}$$

when the first-motion polarities of synthetics and observation are consistent:

$$max\left[cc\left(u_{ijk}^{syn}, u_{ijk}^{obs}\right)\right] + min\left[cc\left(u_{ijk}^{syn}, u_{ijk}^{obs}\right)\right] > 0, \quad (6)$$

where cc is the cross-correlation function. Alvizuri and Tape (2016) suggested the use of the first-motion polarities to reduce uncertainties in the moment tensor solutions.

The waveform fitting between the observed and synthetic from the optimal moment tensor solution for body and surface waves at multiple period bands is shown in Figure 17. Figure 18 shows the distribution of Φ at the lune coordinate (δ, γ) and the global minimum Φ_m suggesting the optimal moment tensor of the September 3, 2017 DPRK nuclear test. Table 3 lists the parameters of the optimal solution from our inversion. The optimal solution falls well in the explosion domain in the lune diagram, while the uncertainty in source type remains large as shown by the 95% confidence limit of the Φ. Adding more stations and with a wider range of epicentral distances (thus a high degree of freedom, equation 2) may reduce the uncertainty.

The isotropic (ISO), compensated linear vector dipole (CLVD) and double couple (DC) components in our moment tensor solution is ~55%, 31% and 14%, respectively. The ISO component is similar to the estimate of Liu et al. (2018, 55-60% ISO component), at the lower end of the estimate of Wang et al. (2018, 50-90% ISO), and substantially less than that of Chiang et al. (2018, 84%). We note that we used a 3D reference model (LITHO1.0, Pasyanos et al., 2014) while all other studies to date used Green's functions of 1D reference models, and Wang et al. (2018) and Chiang et al. (2018) used lower frequency waves in their inversion. Further study is required to understand the discrepancies in the solutions.

Similar searching was carried out for the event 8 minutes after the nuclear test on September 3, 2017. We found that this event contains large implosive component which can be attributed to a collapse following the explosion.

4. CONCLUSIONS

For shallow seismic sources, topography can be the main mechanism that produces scattered waves immediately following the first arrivals. We apply the full waveform location method of Wang et al. (2016) for the first time to real data, using the Non-Proliferation Experiment in the Nevada Test Site as a validation test of the method. By calculating and saving the strain Green's tensor in the grid search volume, we obtain synthetics at the stations using source-receiver reciprocity, which is computationally efficient. We investigate seismograms in two overlapping frequency bands and show that both P and P coda waves are affected significantly by scattering on surface topography (Wang et al., 2019). The solution is robust when different overlapping frequency bands are used for inversion, and insensitive to moderate stochastic velocity heterogeneity perturbations. We conclude that this method is effective for the absolute hypocenter location when applied to real seismic datasets, even though only 12 stations are used and the source-receiver coverage is not ideal (a lack of stations in the y- direction) in the validation test. Further validation of the method for a wide range of topographic roughness and source depth is desirable.

Application of this method to the September 3, 2017 DPRK nuclear test using four stations in China and South Korea yielded a location solution (latitude 41.308°, and longitude 129.067°) within 1 km of the locations of several other studies (Wang et al., 2017a,b). Improvement of the solution can be achieved by incorporating more data from other stations in South Korea and near the DPRK-China border. With greater computational resources, data from stations at larger epicentral distances can also help improve the solution.

Using the Green's functions based on the 3D Earth model LITHO1.0 (Pasyanos et al., 2014) overlying a 1D reference model AK135 (Kennett et al., 1995), we inverted the moment tensor of the September 3, 2017 DPRK nuclear test (Bao et al., 2017). The results show that the isotropic component of the moment tensor is ~55% and there is a significant compensated linear vector dipole (CLVD) component (31%) and a double couple (DC) component (14%).

Tables

Table 1. Uncertainty of the solution at the one standard deviation level (e.q. (2)) for the Non-Proliferation Experiment (NPE) at the Nevada Test Site (NTS).

Data type	Uncertainty of the solution		
	x-direction (km)	y-direction (km)	z-direction (km)
P wave	0.875	1.000	0.311
P and coda wave	0.250	0.875	0.160

Table 2. The 6-D model space of source moment tensor and the settings in searching for the optimal parameters.

parameters	minimum	maximum	interval	number of searching points
moment magnitude (M_w)	M_{w0}-0.1	M_{w0}+0.1	0.02	11
lune latitude (δ_0)	-90	90	10	19
lune longitude (γ_0)	-30	30	10	7
strike (κ)	0	360	10	37
dip (σ)	0	90	10	10
rake (θ)	-90	90	10	19
				Total: 10,284,890

Table 3. Parameters of the optimal moment tensor of the September 3, 2017 DPRK nuclear test.

Lune latitude	60°
Lune longitude	-20°
Moment magnitude (M_w)	5.26
Strike	10°
Dip	10°
Rake	60°
Mrr	9.2025×10^{23} dyne cm
Mtt	5.9863×10^{23} dyne cm
Mpp	5.5177×10^{23} dyne cm
Mrt	-3.0647×10^{23} dyne cm
Mrp	-3.1239×10^{23} dyne cm
Mtp	0.8030×10^{23} dyne cm

Figures

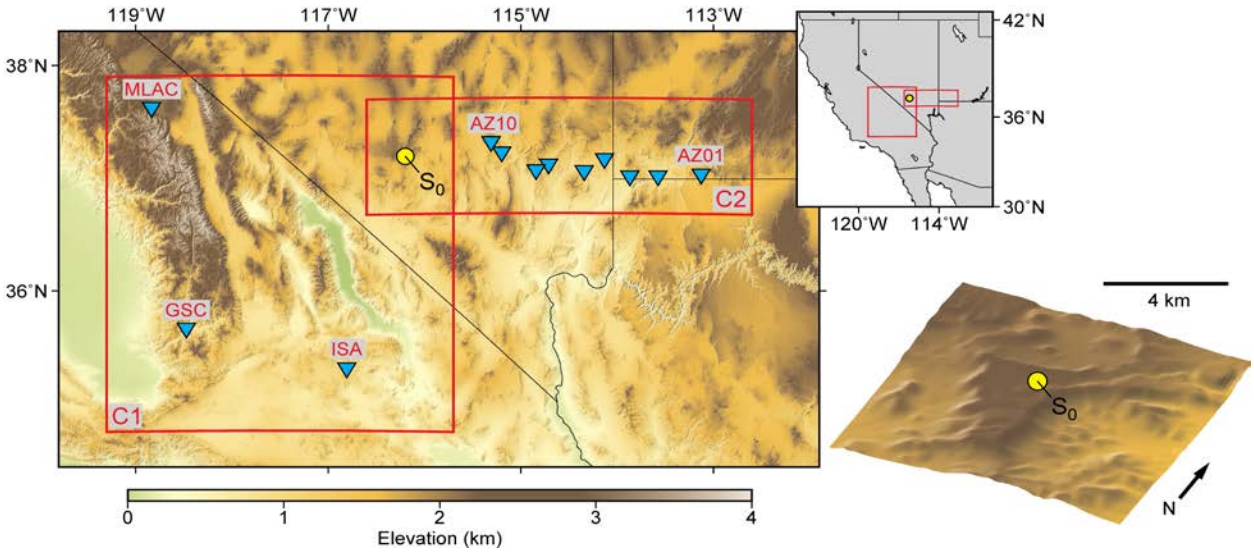

Figure 1. Elevation and distribution of the twelve stations in the two computational regions, and a close-up view showing surface topography of the source region. *The computational region C1 has a dimension of [–132 km, 131.875 km] × [–165 km, 164.875 km] in the horizontal (x-y) plane, where the center is located at longitude x_1=-117.435° and latitude y_1=36.205°. And the computational region C2 has a dimension of [–87.5 km, 87.25 km] × [–80.5 km, 80.25 km] in the horizontal (x-y) plane, where the center is located at longitude x_1=-114.745° and latitude y_1=37.19°. In the linear array of the region C2, station AZ01 is the farthest and station AZ10 is the closest to the exact source (S_0). The bottom right corner of Figure 1 shows the topography near the source and in the grid searching volume, which is 8 km in the x-direction, 10 km in the y-direction and up to 10.4 km in the z- direction.*

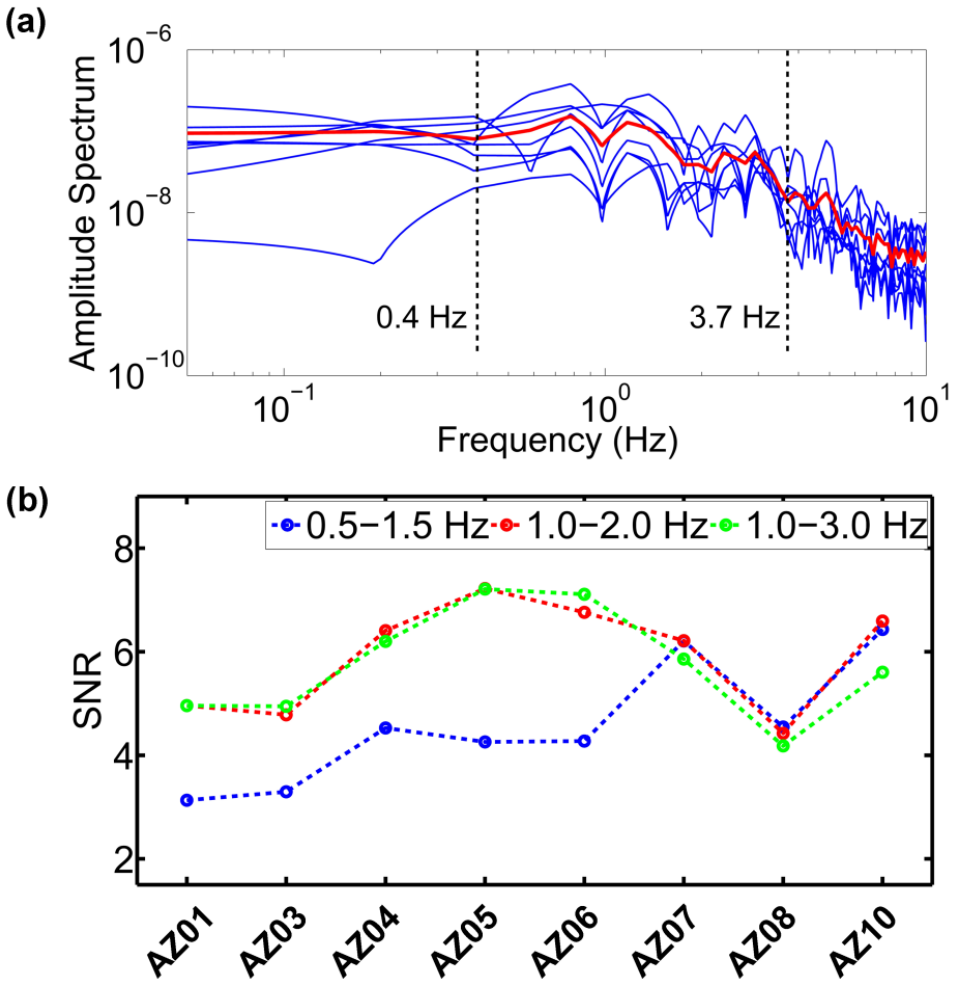

Figure 2. (a) The amplitude spectrum of the vertical component data in the selected time window for the linear array in the computational region C2 (the blue line), and the corresponding averaged amplitude spectrum of the eight stations (the red line). *The time window for each station starts from the first arrival time and is with a length of three seconds.* (b) The signal-noise-ratio of the vertical component data for the eight stations at different frequency bands. *The time window of the noise is five seconds before the first arrival time and the time window of the signal is three seconds after the first arrival time.*

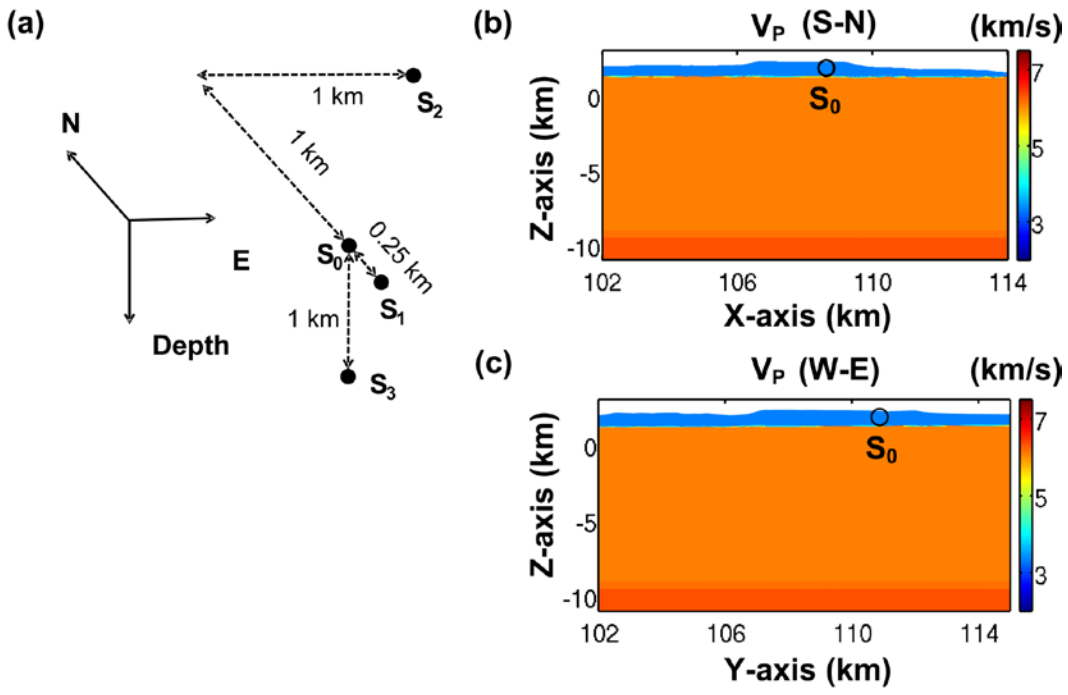

Figure 3. (a) Relative locations of four test sources, where S_0 marks at the true location, and (b) the slices of P- wave velocity around S_0 cut vertically along the South-North direction (in the y-z plane) and cut vertically along the West-East direction (in the x-z plane) in the reference model.

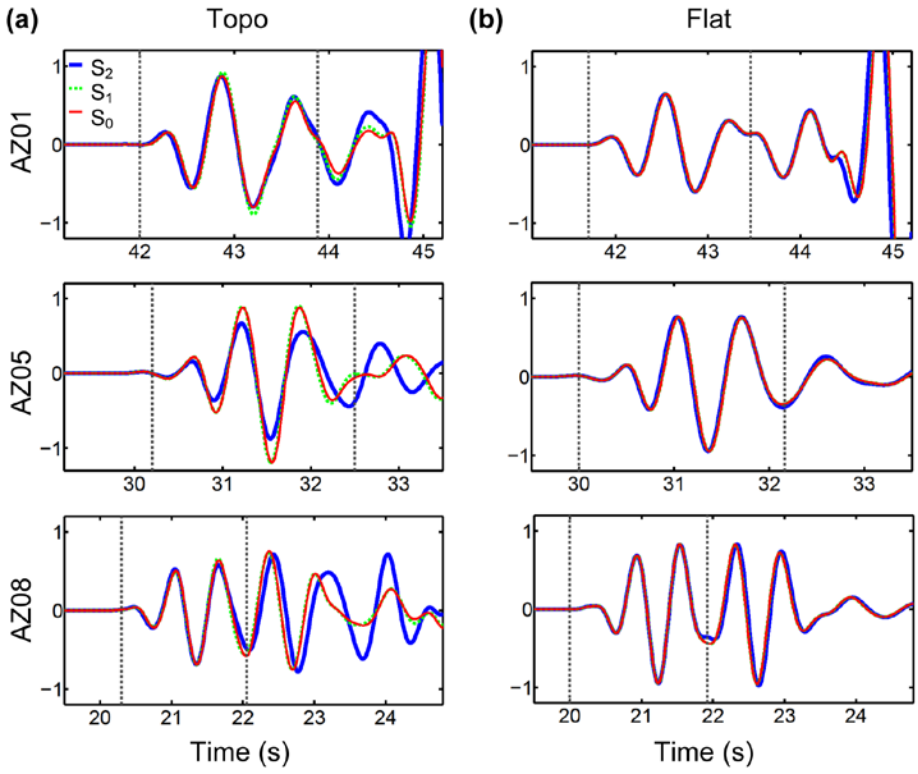

Figure 4. The comparison of vertical-component displacement seismograms generated by the three test sources (locations are varied in the horizontal x-y direction) at three stations, in the velocity models with (a) and without (b) topography.

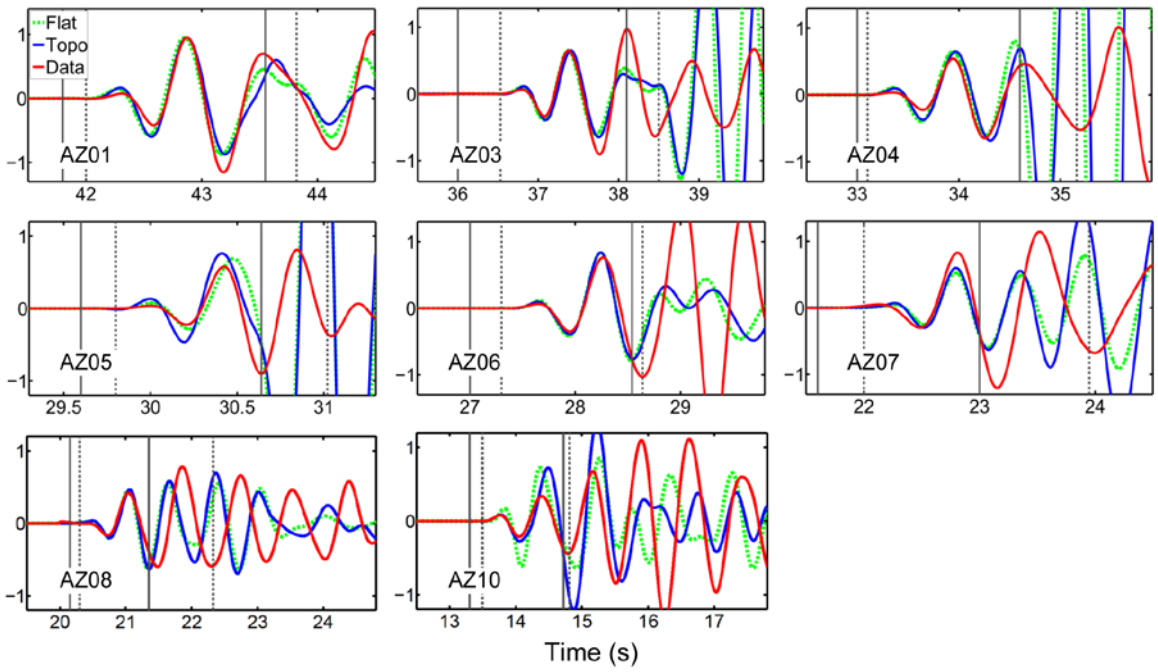

Figure 5. The comparison of vertical-component seismograms at eight stations between the data (the red line) and synthetics generated by the source located at S_0 in the velocity models with (the blue line) and without (the green line) topography.

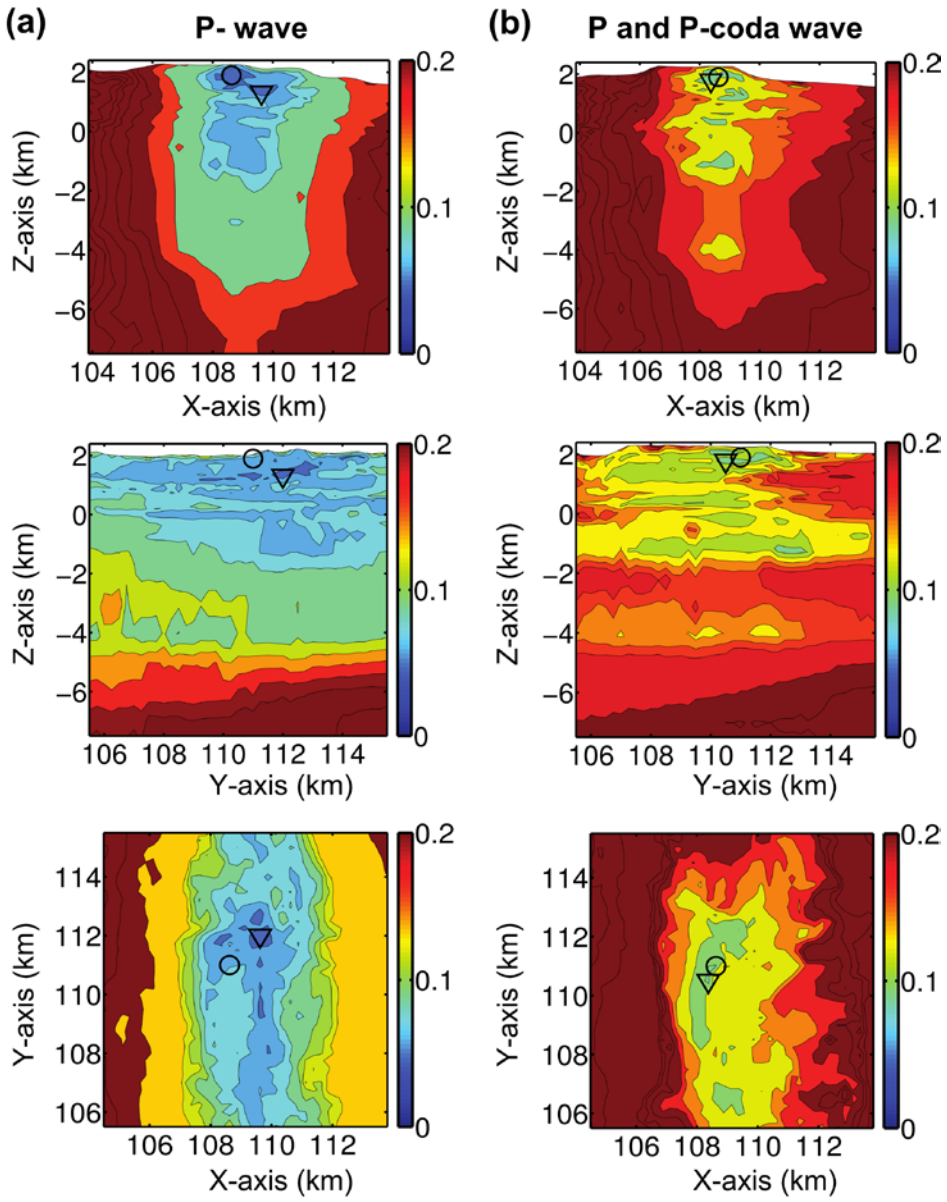

Figure 6. Contour plots of the misfit E for test sources in three orthogonal planes in the grid search volume V, cut at the grid point with the minimum value, in the x-z plane (top), the y-z plane (middle) and the x-y plane (bottom), by using only P waves (a) and P and P- coda waves (b), respectively. *The circle is the exact source S_0 located at (108.625 km, 110.75 km, 1.92 km). The inverted triangle is the best solution for each case located at (109.63 km, 112 km, 1.31 km) in Figure a and at (108.38 km, 110.5 km, 1.78 km) in Figure b. The coordinate is based on that of the region C1. The frequency band used to filter the data and synthetics is [1 2] Hz.*

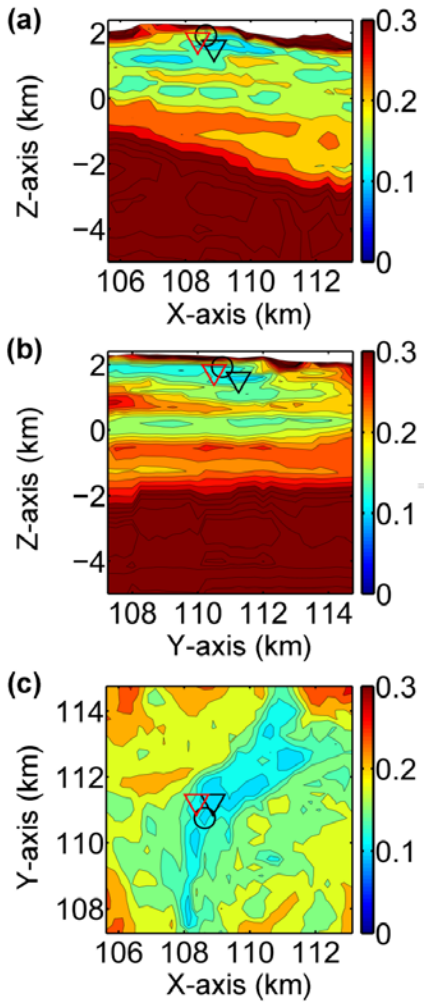

Figure 7. Contour plots of the misfit E for test sources in three orthogonal planes in the grid search volume V, cut at the grid point with the minimum value, in the x-z plane (a), the y-z plane (b) and the x-y plane (c), by using P and P- coda waves, respectively. *The frequency band used to filter the data and synthetics is [1-3] Hz. The black circle is the exact source S_0 located at (108.625 km, 111.0 km, 1.89 km). The black inverted triangle is the best solution with 1-3 Hz signals (located at 108.88 km, 111.25 km, 1.559 km). For comparison, the red inverted triangle is the best solution with 1-2 Hz signals (located at 108.38 km, 110.5 km, 1.78 km, Figure 5b). The coordinate is based on that of the region C1.*

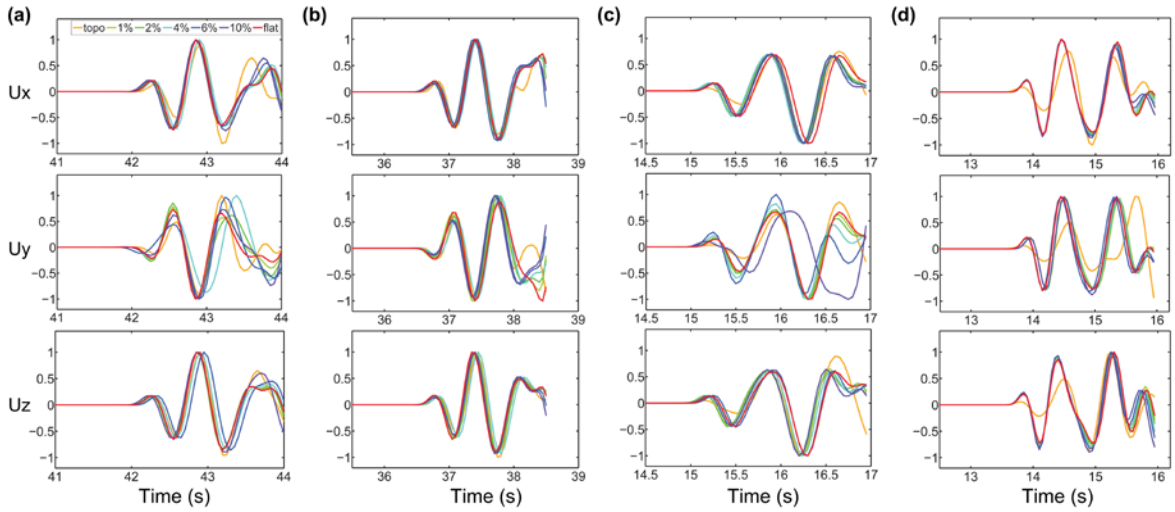

Figure 8. Normalized three-component synthetic displacement seismograms at stations (a) AZ01, (b) AZ03, (c) AZ09, and (d) AZ10. *The synthetics are computed for the models with different perturbation percentages of P- and S-wave velocities (1%-10%) based on the flat model. The seismograms for the models with (orange line) and without (red line) topography but no stochastic velocity perturbations are shown for comparison. The source is located at* S_1.

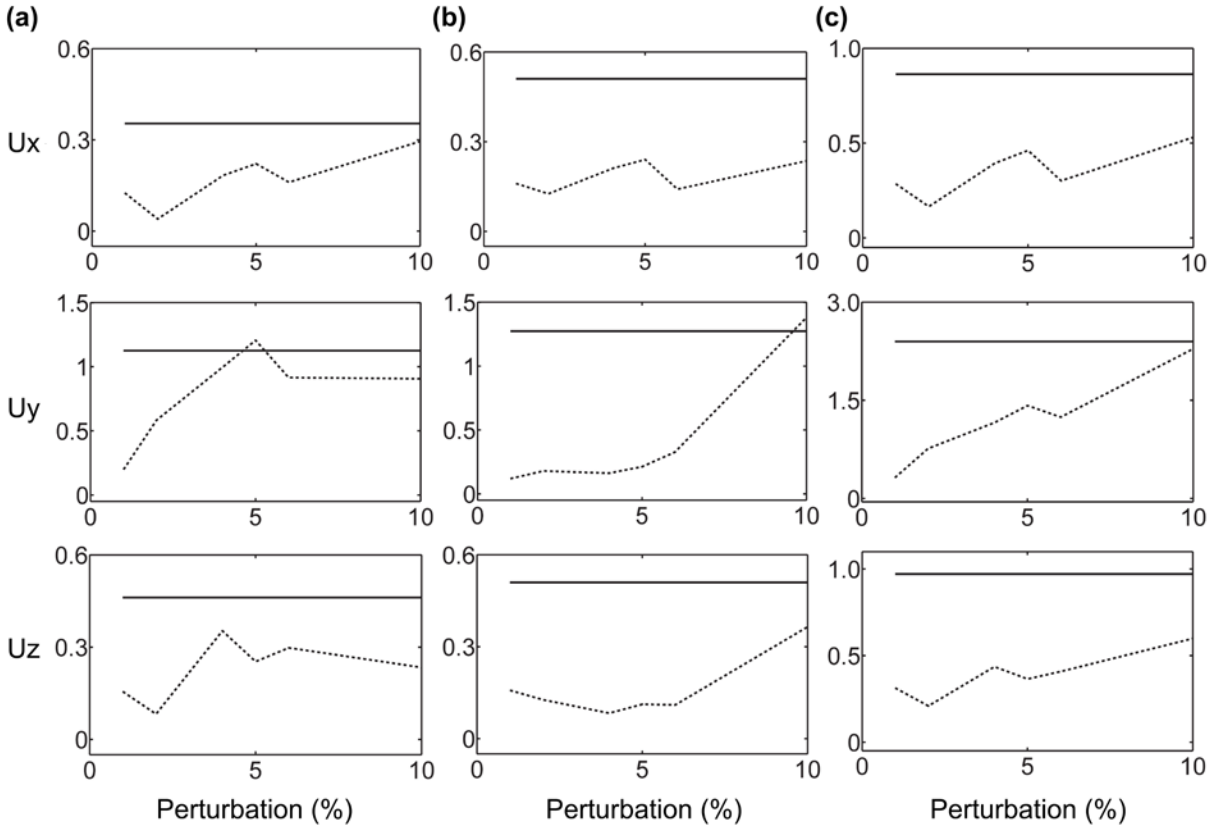

Figure 9. Comparison of the three-component waveform misfit (eq. (1)) due to surface topography (the solid black line) with those of velocity heterogeneities perturbations in percentage (the dash black line), for (a) Pn and Pn coda waves at eight stations, (b) Pg and Pg coda waves at four stations, and (c) the first arrivals and their coda waves at all the twelve stations. *The source is located at* S_1.

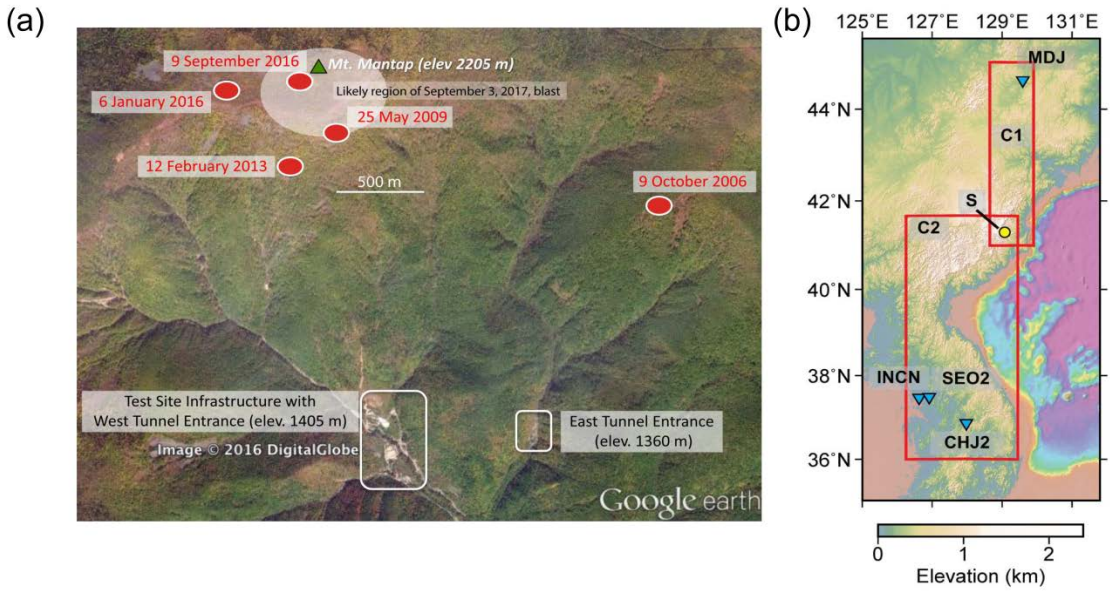

Figure 10. (a) The North Korea nuclear test site (from the NORSAR solution), and (b) our study region and distribution of stations used for the full waveform location inversion. *The yellow circle marks the Punggye-ri test sites.*

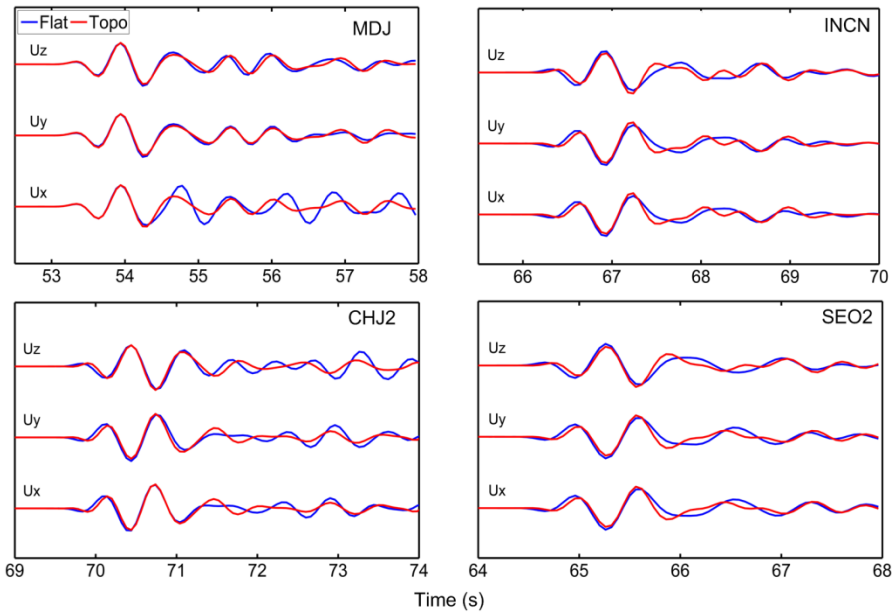

Figure 11. Comparison of seismograms at the four stations between synthetic simulations in the model with (the ′red′ line) and without (the ′blue′ line) topography.

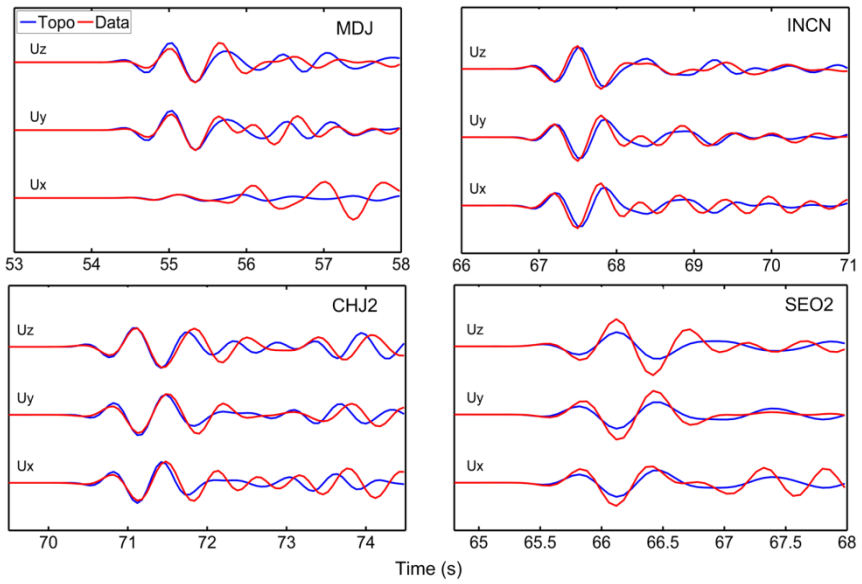

Figure 12. Comparison of seismograms at the four stations between the data (the ′red′ line) and the synthetics in the topographic model (the ′blue′ line).

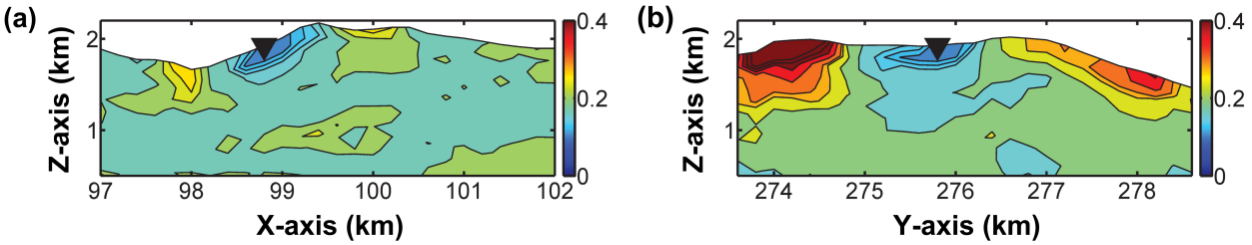

Figure 13. The contour plots of the P and P coda wave misfit between the observed and synthetics for the September 3, 2017 event in the x-z plane (with y=275.8 km) (a) and y-z plane (with x=98.8 km) (b), cut at the location of the best solution (triangle, with x=98.8 km, y=275.8 km, and z=1.924 km).

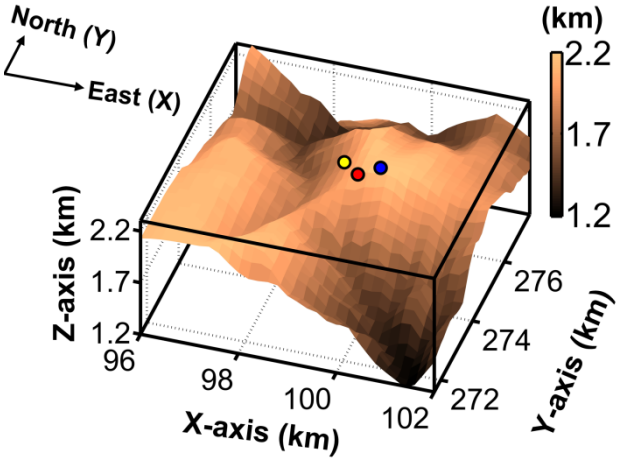

Figure 14. 3D view of the epicenter locations of the September 3, 2017 test determined by modeling P and topography scattered waves (yellow point, at latitude 41.308°, and longitude 129.067°). *The corresponding USTC solution (red point, at latitude 41.2982°, and longitude 129.0742°) and NORSAR solution (blue point, at latitude 41.2994°, and longitude 129.0789°) based on relative travel times are also shown for comparison.*

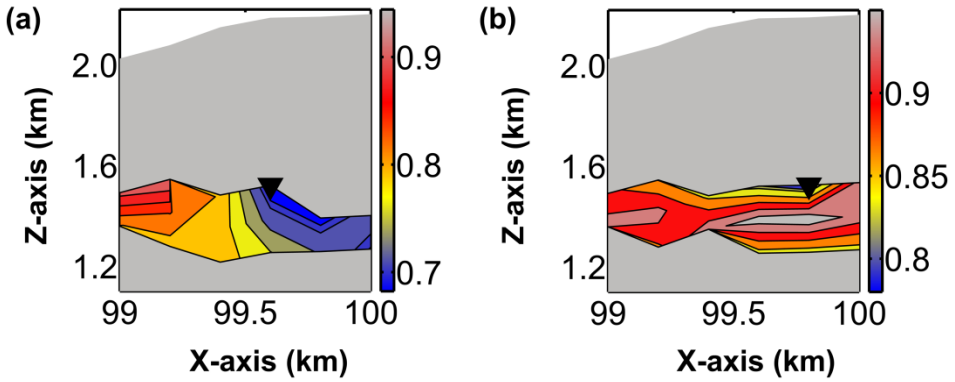

Figure 15. Misfit of the double differential waveform inversion between the September 3, 2017 test and the September 9, 2016 test. *We limit the search region around the mountain in the North Korea test site and in an elevation range close to the elevation of the tunnel entrance (See Figure 10). For each possible location of the 2017 event, we find all the possible locations of the 2016 event and record the corresponding minimum double differential waveform misfits of the two events. After going through all possible grid points of the 2017 event in the search region, we obtain the best solution of the 2017 event (with x=99.6 km, y=274.8 km, and z=1.52 km (approximately 800 m below the surface)), and show the misfit cut at the best solution in the x-z plane (a). Similarly, for each possible location of the 2016 event, we can find the corresponding misfit in the search region, obtain the best solution (with x=99.8 km, y=274.8 km, and z=1.52 km), and show the misfit cut at the best solution in the x-z plane (b).*

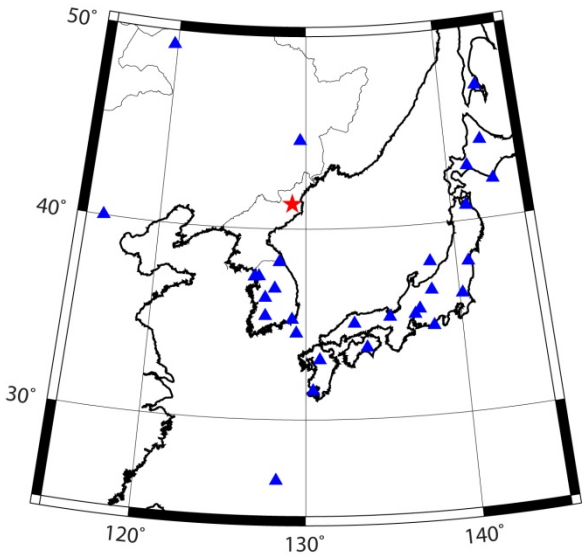

Figure 16. Map of the DPRK test site (red star) and the stations (blue triangles) recording the broadband waveform data used in the full-wave moment tensor study.

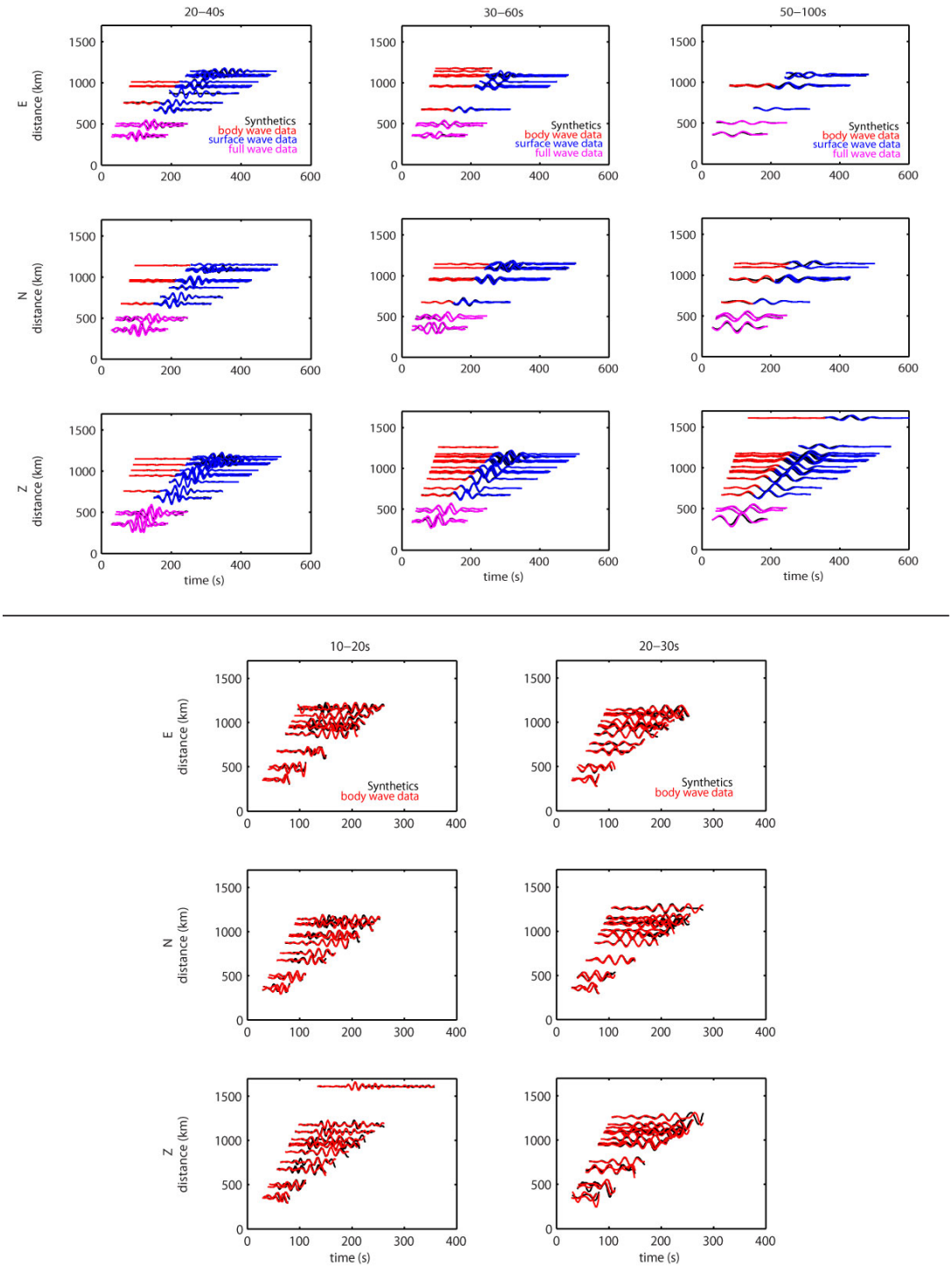

Figure 17. Three-component waveform fitting between data and synthetics from the optimal moment tensor solution. *The three columns on the top half and the two columns on the bottom half show the waveform fitting of body and surface waves at different period bands.*

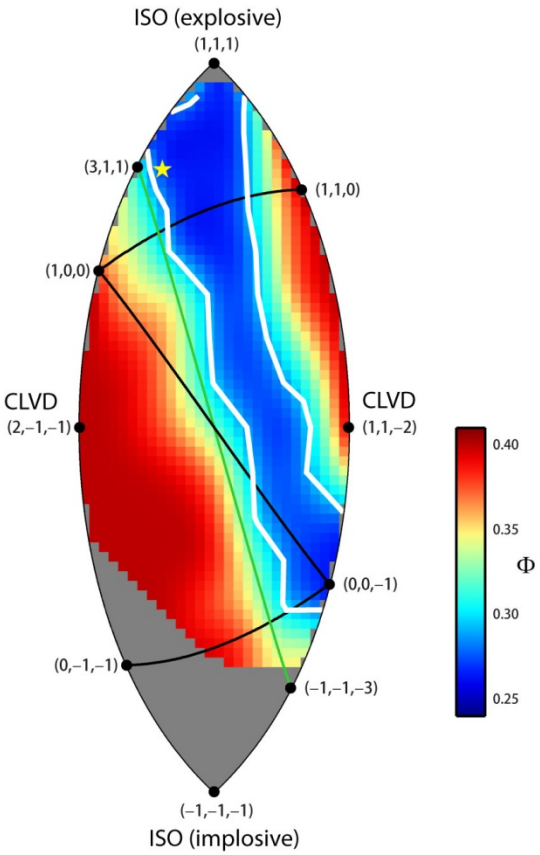

Figure 18. Distribution of Φ at the lune coordinate. *Yellow star shows the global minimum Φ_m, suggesting the optimal moment tensor of the September 3, 2017 DPRK nuclear test. White lines denote the 95% confidence interval of the solution. The gray area around the bottom of the lune diagram represents the source parameters not correctly predicting the first-motion polarities.*

REFERENCES

Alvizuri, C. and C. Tape (2016), Full moment tensors for small events (Mw<3) at Uturuncu volcano, Bolivia, Geophys. J. Int., 206, pp. 1761-1783, doi: 10.1093/gji/ggw247.

Bao, X., Y. Shen, and N. Wang (2017), Moment Inversion of the DPRK Nuclear Tests Using Finite-Difference Three-dimensional Strain Green's Tensors, abstract S43H-2964, presented at the Fall AGU meeting, New Orleans, 11-15 December 2017.

Brown, R. J., G. H. Friesen, D. H. Hall, and O. G. Stephenson (1977), Weighted vertical stacking in crustal seismic reflection studies on the Canadian shield, Geophys. Prospect., 25(2), pp. 251-268.

Chiang, A., G.A. Ichinose, D.S. Dreger, S.R. Ford, E.M. Matzel, S.C. Myers, and W.R. Walter (2018), Moment tensor source-type analysis for the Democratic People's Republic of Korea – declared nuclear explosions (2006-2017) and 3 September 2017 collapse event, Seismol. Res. Lett., doi:10.1785/0220180130.

Crotwell, H. P., T. J. Owens, and J. Ritsema (1999), The TauP Toolkit: Flexible seismic travel-time and ray-path utilities, Seismol. Res. Lett., 70, pp. 154-160.

Denny, M.D. and J.J. Zucca (1994), Introduction: DOE Non-Proliferation Experiment, in Arms Control and Nonproliferation Technologies, First Quarter 1994, pp. 8-21.

Draper, N. R. and H. Smith (1966), Applied Regression Analysis, Wiley, New York.

Ford, S. R., D. S. Dreger, and W. R.Walter (2009), Identifying isotropic events using a regional moment tensor inversion, J. Geophys. Res. 114, no. B01306, doi: 10.1029/2008JB005743.

Goff, J. A., K. Holliger, and A. Levander (1994), Modal fields: A new method for characterization of random seismic velocity heterogeneity, Geophys. Res. Lett., 21(6), pp. 493-496.

Gupta, I. N., T. W. McElfresh, and R. A. Wagner (1991), Near-Source Scattering of Rayleigh to P in Teleseismic Arrivals from Pahute Mesa (NTS) Shots, in Explosion Source Phenomenology, eds Taylor, S. R., Patton, H. J., & Richards, P. G., American Geophysical Union, Washington, D. C.

Imperatori, W. and P. M. Mai (2015), The role of topography and lateral velocity heterogeneities on near-source scattering and ground-motion variability, Geophys. J. Int., 202, pp. 2163-2181, doi:10.1093/gji/ggv281.

Kennett, B. L. N. (1987), Observational and theoretical constraints on crustal and upper mantle heterogeneity, Phys. Earth Planer Int., 47, pp. 319-332.

Kennett, B.L.N., E.R. Engdahl, and R. Buland (1995), Travel times for global earthquake location and phase association, Geophys. J. Int., 122, pp. 108-124, doi: 10.1111/j.1365-246X.1995.tb03540.x.

Kikuchi, M. and H. Kanamori (1991), Inversion of complex body waves-III, Bull. Seism. Soc. Am., 81, pp. 2335-2350.

Laske, G., G. Masters., Z. Ma, and M. Pasyanos (2013), Update on CRUST1.0 – A 1-degree Global Model of Earth's Crust, Geophys. Res. Abstracts, 15.

Lerosey, G., J de Rosny, A. Tourin, and M. Fink (2007), Focusing beyond the diffraction limit with far-field time reversal, Science, 315, pp. 1120-1122.

Liu, J., L. Li, J. Zahradnik, E. Sokos, C. Liu, and X. Tian (2018), North Korea's 2017 Test and its nontectonic aftershock, Geophysical Research Letters, 45, pp. 3017-3025, https://doi.org/10.1002/2018GL077095.

Lomax, A., A. Michelini, and A. Curtis (2008), Earthquake location, direct, global-search methods, in Encyclopedia of Complexity and System Science, pp. 2449-2473, ed. Meyers, R. A. Springer, New York.

Murphy, J. R., J. L. Stevens, B. C. Kohl, and T. J. Bennett (2013), Advanced seismic analyses of the source characteristics of the 2006 and 2009 North Korean nuclear tests, Bull. Seismol. Soc. Am., 103, pp. 1640-1661, doi: 10.1785/0120120194.

NORSAR solution: https://www.norsar.no/press/latest-press-release/archive/large-nuclear-test-in-north-korea-on-3-september-2017-article1534-984.html, last accessed 09/04/2017.

O'Brien, G. S., and C. J. Bean (2009), Volcano topography, structure and intrinsic attenuation: Their relative influences on a simulated 3D visco-elastic wavefield, J. Volc. Geotherm. Res., 183(1-2), pp. 122-136.

Pasyanos, M.E., T.G. Masters, G. Laske, and Z. Ma (2014), LITHO1.0: An updated crust and lithospheric model of the Earth, J. Geophys. Res., 119 (3), pp. 2153-2173, doi: 10.1002/2013JB010626.

Pasyanos, M. E. and S. C. Myers (2018), The coupled location/depth/yield problem for North Korea's declared nuclear tests, Seismol. Res. Lett. doi: 10.1785/0220180109.

Rodgers, A. J., N. Anders Petersson, and B. Sjogreen (2010), Simulation of topographic effects on seismic waves from shallow explosions near the North Korean nuclear test site with emphasis on shear wave generation, J. Geophys. Res., 115, B11309.

Sambridge, M. S. and B. L. N. Kennett (1986), A novel method of hypocentre location, Geophys. J. Int., 87(2), pp. 679-697.

Schaff, D. P. and P. G. Richards (2004), Repeating seismic events in China, Science 303, pp. 1176-1178, doi: 10.1126/science.1093422.

Selby, N. D. (2010), Relative locations of the October 2006 and May 2009 DPRK announced nuclear tests using international monitoring system seismometer arrays, Bull. Seismol. Soc. Am. 100, pp. 1779-1784, doi: 10.1785/0120100006.

Stead, R. J. and D. V. Helmberger (1988), Numerical-analytical interfacing in two dimensions with applications to modeling NTS seismograms, Pure Appl. Geophys., 128, pp. 157-193.

Stevens, J.L. and M. O'Brien (2018), 3D nonlinear calculation of the 2017 North Korean nuclear test, Seismol. Res. Lett., doi:10.1785/0220180099.

Takemura, S., T. Furumura, and T. Maeda (2015), Scattering of high-frequency seismic waves caused by irregular surface topography and small-scale velocity inhomogeneity, Geophys. J. Int., 201, pp. 459-474.

Tape, W. and C. Tape (2012), A geometric comparison of source-type plots for moment tensors, Geophys. J. Int., 190, pp. 499-510, doi: 10.1111/j.1365-246X.2012.05490.x.

Tinker, M. A. and T. C. Wallace (1997), Regional phase development of the Non-Proliferation Experiment within the Western United States, Bull. Seism. Soc. Am., 87(2), pp. 383-395.

USTC solution:http://seis.ustc.edu.cn/_s223/2017/0904/c10084a191096/page.psp, last accessed 09/04/2017.

Waldhauser, F. and Ellsworth, W. L. (2000), A double-difference earthquake location algorithm: Method and application to the northern Hayward fault, California, Bulletin of the Seismological Society of America, 90(6), pp. 1353-1368.

Wen, L. X. and H. Long (2010), High-precision location of North Korea's 2009 nuclear test, Seismol. Res. Lett. 81, pp. 26-29, doi: 10.1785/gssrl.81.1.26.

Wang, N., X. Bao, and Y. Shen (2017a), Location of the Sept. 3, 2017 North Korea nuclear test from full-wave modeling, IRIS special Event: 2017 North Korean nuclear test, https://ds.iris.edu/ds/nodes/dmc/specialevents/2017/09/03/2017-north-korean-nuclear-test/.

Wang, N., Y. Shen, X. Bao, and A.F. Flinders (2017b), Pinpointing the North Korea Nuclear tests with body waves scattered by surface topography, abstract S43H-2972, presented at the Fall AGU meeting, New Orleans, 11-15 December 2017.

Wang, N., Y. Shen, X. Bao, and A.F. Flinders (2019), Locating shallow seismic sources with waves scattered by surface topography: Validation of the method at the Nevada Test Site, J. Geophys. Res. Solid Earth, doi: 10.1029/2018JB017291.

Wang. N., Y. Shen, A. Flinders, and W. Zhang (2016), Accurate source location from waves scattered by surface topography, J. Geophys. Res., 121(6), pp. 4538-4552.

Wang, T., Q. Shi, M. Nikkhoo, S. Wei, S. Barbot, D. Dreger, R. Burgmann, M. Motagh, and Q.F. Chen (2018), The rise, collapse, and compaction of Mt. Mantap from the 3 September 2017 North Korean nuclear test, Science, 10.1126/science.aar7230.

Zhang, W., and X. F. Chen (2006). Traction image method for irregular free surface boundaries in finite difference seismic wave simulation, Geophys. J. Int., 167, 337-353.

Zhang, W., Z. Zhang, and X. Chen (2012), Three-dimensional elastic wave numerical modelling in the presence of surface topography by a collocated-grid finite-difference method on curvilinear grids, Geophys. J. Int., 190(1), pp. 358-378.

Zhao, L., P. Chen, and T. H. Jordan (2006), Strain Green's tensor, reciprocity, and their applications to seismic source and structure studies, Bull. Seism. Soc. Am., 96, pp. 1753-1763.

Zhao, L. F., X. B. Xie, W. M. Wang, J. L. Hao, and Z. X. Yao (2016), Seismological investigation of the 2016 January 6 North Korean underground nuclear test, Geophys. J. Int. 206, pp. 1487-1491, doi:10.1093/gji/ggw239.

Zhao, L. F., X. B. Xie, W. M. Wang, and Z. X. Yao (2014), The 12 February 2013 North Korean underground nuclear test, Seismol. Res. Lett. 85, pp. 130-134, doi: 10.1785/0220130103.

Zhou, L., W. Zhang, Y. Shen, X. Chen, and J. Zhang (2016), Location and moment tensor inversion of small earthquakes using 3D Green’s functions in models with rugged topography: application to the Longmenshan fault zone, Earthq. Sci., 29(3), pp. 139-151, doi: 10.1007/s11589-016-0156-1.

Zhu, L. and D.V. Helmberger (1996), Advancement in source estimation techniques using broadband regional seismograms, Bull. Seismol. Soc. Am., 86 (5), pp. 1634-1641.

List of Symbols, Abbreviations, and Acronyms

AFRL	Air Force Research Laboratory
AFSPC	Air Force Space Command
AFWA	Air Force Weather Agency
AGU	American Geophysical Union
CLVD	Compensated Linear Vector Dipole of the moment tensor
DC	Double Couple component of the moment tensor
DPRK	Democratic People's Republic of Korea
IRIS	Incorporated Research Institutions for Seismology
ISO	Isotropic component of the moment tensor
NPE	Non-Proliferation Experiment
NORSAR	Norwegian Seismic Array
PSD	Power spectral density
SGT	Strain Green Tensor
USTC	University of Science and Technology of China

DISTRIBUTION LIST

DTIC/OCP
8725 John J. Kingman Rd, Suite 0944
Ft Belvoir, VA 22060-6218 1 cy

AFRL/RVIL
Kirtland AFB, NM 87117-5776 1 cy

Official Record Copy
AFRL/RVB/Dr. Frederick Schult 1 cy